Simultaneous oxidation of Hg^0 and NH_3-SCR of NO by nanophase $Ce_xZr_yMn_zO_2$ at low temperature: the interaction and mechanism

By: Wanrong Wu, Zheng Zeng, Pei Lu, Yi Xing, Jianjun Wei, Huifang Yue, and Rui Li

W. Wu, Z. Zeng, P. Lu, Y. Xing, J. Wei, H. Yue, R. Li, Simultaneous oxidation of Hg^0 and NH_3-SCR of NO by nanophase $Ce_xZr_yMn_zO_2$ at low temperature: the interaction and mechanism. *Environmental Science and Pollution Research*, **2018** 25 (15), 14471-14485. DOI:10.1007/s11356-018-1657-3.

Abstract:

Simultaneous oxidation of Hg^0 and NH_3-SCR of NO by catalyst is one of the key methods for co-purification of coal-fired flue gas. Till now, the interaction between the oxidation of Hg^0 and NH_3-SCR of NO and its mechanism have not clarified. In this study, a series of nanophase $Ce_xZr_yMn_zO_2$ was prepared for the simultaneous oxidation of Hg^0 and NH_3-SCR of NO at low temperature. The catalysts were characterized using surface area analysis, X-ray diffraction, temperature-programmed techniques, and several types of microscopy and spectroscopy. The experimental results indicated that the $Ce_{0.47}Zr_{0.22}Mn_{0.31}O_2$ exhibited superior Hg^0 removal efficiency (> 99%) and NO conversion efficiency (> 90%) even at 150 °C, and it also exhibited a good durability in the presence of SO_2 and H_2O. The excellent performance of $Ce_{0.47}Zr_{0.22}Mn_{0.31}O_2$ on co-purifying Hg^0 and NO was due to the stronger synergistic effects of Ce-Zr-Mn in $Ce_{0.47}Zr_{0.22}Mn_{0.31}O_2$ than that of the others, which was illustrated by the characterization results of XPS, XRD, and FT-IR. Moreover, it was found that the NO conversion of $Ce_{0.47}Zr_{0.22}Mn_{0.31}O_2$ could be slightly influenced by Hg^0 and was decreased about 4% to the max, while that of Hg^0 could rarely be affected by the selected catalytic reduction process of NO. It might be due to the co-purification mechanism of NO and Hg^0. The mechanism of the simultaneous oxidation of Hg^0 and NH_3-SCR of NO was mainly due to the synergetic effect on the mobility of surface oxygen and the activation of lattice oxygen of $Ce_{0.47}Zr_{0.22}Mn_{0.31}O_2$. The effect of the oxidation of Hg^0 on the NH_3-SCR of NO was mainly due to the absorbed Hg^0/Hg^{2+} on the surface of $Ce_{0.47}Zr_{0.22}Mn_{0.31}O_2$, which attenuated the formation of $NH_{3(ad)}$, $-NH_{2(ad)}$, and NH_4^+ on its acid sites. Similarly, the NH_3-SCR of NO process could hardly influence the oxidation of Hg^0 when NO and Hg^0 were co-purified.

Keywords: Oxidation of Hg^0 | NH_3-SCR of NO | Low temperature | Nanophase $Ce_xZr_yMn_zO_2$ | Interaction and mechanism

Article:

Introduction

The emission of NO_x, which consists of over 90–95% NO, and elemental mercury (Hg^0) from coal combustion has attracted broad attention in recent years (Zhao et al. 2016b; Zheng et al. 2007). NO_x can cause a series of environmental problems, such as acid rain, photochemical smog, and haze formation (Lian et al. 2014; Wang et al. 2015). Mercury can do harm to both the environment and human health because of its extreme toxicity, persistence, and bioaccumulation of its compounds (Yuan et al. 2012). Therefore, it is very important to co-purify NO_x and Hg^0 from flue gas for human health and environmental protection (Zhao et al. 2015; Xie et al. 2013).

Until now, selective catalytic reduction (SCR) has been considered to be the most effective process used to remove NO. For Hg^0 removal, activated carbon injection (ACI) systems are the most effective available technologies (Sjostrom et al. 2010; Liu et al. 2017). However, the large activated carbon consumption of ACI and the high investment and operating costs involved in controlling the two emissions separately have led researchers to develop a new technology to purify NO and Hg^0 simultaneously (Fang et al. 2013; Zhang et al. 2017a). The catalysts used in SCR of NO have the co-benefit of facilitating Hg^0 oxidation (Chi et al. 2017; Zhang et al. 2015c; Zhang et al. 2013, 2017a, b). However, most of the catalysts used in SCR systems show the best catalytic activity in NO conversion around 300 to 400 °C, which was not the best temperature for Hg^0 oxidation. Furthermore, the conversion of SO_2 to SO_3 is high, and the selectivity of N_2 is low in the high-temperature range (Yang et al. 2011; Ettireddy et al. 2007; Smirniotis et al. 2001). Therefore, a catalyst that can simultaneously remove NO and Hg^0 at low temperature needs to be investigated.

Recently, CeO_2 was extensively researched in Hg^0 oxidation and NO conversion because it showed good capability of storing and releasing oxygen (Bin et al. 2014; Fan et al. 2012). The conversion process between Ce^{4+} and Ce^{3+} under oxidizing or reducing conditions can produce highly reactive oxygen vacancies and unsaturated chemical bonds, which have high activity to participate in catalytic reaction (Liu et al. 2013; Wen et al. 2011). With the addition of Zr, the dispersion of CeO_2 and MnO_2 can be improved (Song et al. 2016). Moreover, the insertion of ZrO_2 into CeO_2 improves the mobility of lattice oxygen and the density of oxygen vacancies, because part of the Ce^{4+} in CeO_2 is replaced by Zr^{4+} to form the cubic fluorite structure of Ce-Zr mixed oxides (Zhao et al. 2016a). MnO_2 has also shown high activity for NO reduction with NH_3 at low temperatures (Ettireddy et al. 2007). Besides, doping metal oxides can enhance NO_x conversion and N_2 selectivity of manganese oxide-based catalysts in low-temperature NH_3-SCR (Boningari and Smirniotis 2016; Li et al. 2011). Recently, Ce-Ti-, Ce-Zr-, and Ce-Mn-based catalysts were studied for Hg^0 oxidation, NO conversion, and simultaneous removal of NO and Hg^0 (Wang et al. 2015; Chi et al. 2017; Reddy et al. 2015; Ding et al. 2015; Lei et al. 2008). For example, Zhao et al. investigated the simultaneous removal of NO and Hg^0 from flue gas over Mn-Ce/Ti-PILCs (PILCs, pillared interlayered clays) catalysts (Wang et al. 2015). He et al. found that MnO_x/TiO_2, MnO_x/CeO_2-TiO_2, and CeO_2-TiO_2 materials exhibit excellent NO removal performance and high Hg^0 adsorption capacities both in single-component (NO or Hg^0) tests and in combined NO and Hg^0 removal experiments at 175 °C (He et al. 2013). However, Ce-Zr-Mn mixed oxides focusing on the synergistic effects of Ce and Mn have seldom been

reported for co-purifying NO and Hg^0 at low temperature. Moreover, the interaction between Hg^0 and NO when they are simultaneously purified and the mechanism have not been clarified.

Therefore, series of nanophase $Ce_xZr_yMn_zO_2$ catalysts were prepared for the simultaneous oxidation of Hg^0 and NH_3-SCR of NO at low temperature in this study. Based on the performance on co-purifying of NO and Hg^0 at low temperature and the characterization of the physicochemical properties of the catalysts, the interaction of the oxidation of Hg^0 and the NH_3-SCR of NO and its mechanism were specially studied in this study.

Experimental

Catalyst preparation

The $Ce_xZr_yMn_zO_2$ catalysts employed in this study were synthesized in one-pot. $Ce(NO_3)_3{\cdot}6H_2O$, $ZrO(NO_3)_2$, and $Mn(NO_3)_2{\cdot}4H_2O$ were used as precursors and were dissolved in deionized water. The solutions were heated in a water bath at 80 °C with continuous stirring for 1 h to attain uniform mixing. After the solution cooled to room temperature, an ammonia solution was added dropwise into the obtained solution under vigorous stirring until the pH arrived at 10. The resulting precipitates were stirred for 3 h and then aged for 1 h, and finally filtered, washed, and dried at 80 °C overnight. Then, the samples were calcined at 500 °C for 5 h in a muffle furnace. The mixed metal oxide solids were prepared in five different molar ratios: $Ce_{0.12}Zr_{0.17}Mn_{0.71}O_2$, $Ce_{0.16}Zr_{0.22}Mn_{0.62}O_2$, $Ce_{0.23}Zr_{0.32}Mn_{0.45}O_2$, $Ce_{0.37}Zr_{0.26}Mn_{0.37}O_2$, and $Ce_{0.47}Zr_{0.22}Mn_{0.31}O_2$.

Catalyst characterization

The Brunauer-Emmett-Teller (BET) surface area, average pore size, and pore volume of the catalysts were obtained from the adsorption and desorption of N_2 at liquid nitrogen temperature (− 196 °C) using a Micromeritics Tristar II 3020 analyzer (Micromeritics Instrument Corp., Norcross, GA, USA). The specific surface area was calculated by the BET method, and the pore volume and average pore size were evaluated by the Barrett-Joiner-Halenda method.

The transmission electron microscopy (TEM) images of the samples were collected on a JEOL JEM-2100 electron microscope (JEOL Ltd., Tokyo, Japan) at 200 kV to evaluate the particle size and morphology of the catalysts.

Fourier transform infrared (FT-IR) spectroscopy was performed using a Bruker Equinox 55 FT-IR spectrometer (Bruker Optics, Ettlingen, Germany) to measure the surface groups of the catalysts. The spectral region between 400 and 4000 cm^{-1} was scanned with a 2-cm^{-1} resolution.

X-ray diffraction (XRD) measurements were carried out by a Rigaku D/max-2500 powder diffractometer (Rigaku, Tokyo, Japan) with Cu Kα radiation (40 kV, 200 mA). The scanning range was 10° to 80° (2θ), with a step size of 0.02° and a scanning rate of 8° min^{-1}.

X-ray photoelectron spectroscopy (XPS) measurements were carried out using an ESCALAB 250Xi (Thermo Fisher Scientific, MA, USA) with a monochromatic Al Kα X-ray source (1486.6 eV). The binding energies were calibrated using the C1s photoelectron peak at 284.6 eV.

Temperature-programmed reduction of H_2 (H_2-TPR) and the temperature-programmed desorption of NH_3 (NH_3-TPD) were conducted on a Micromeritics AutoChem II 2920 (Micromeritics Instrument Corp.) with 200-mg samples to obtain surface acidity.

Catalytic activity test

The catalytic activity measurements for Hg^0 oxidation and NO conversion were carried out in a fixed-bed reactor. The schematic diagram of the experimental setup is shown in Fig. 1.

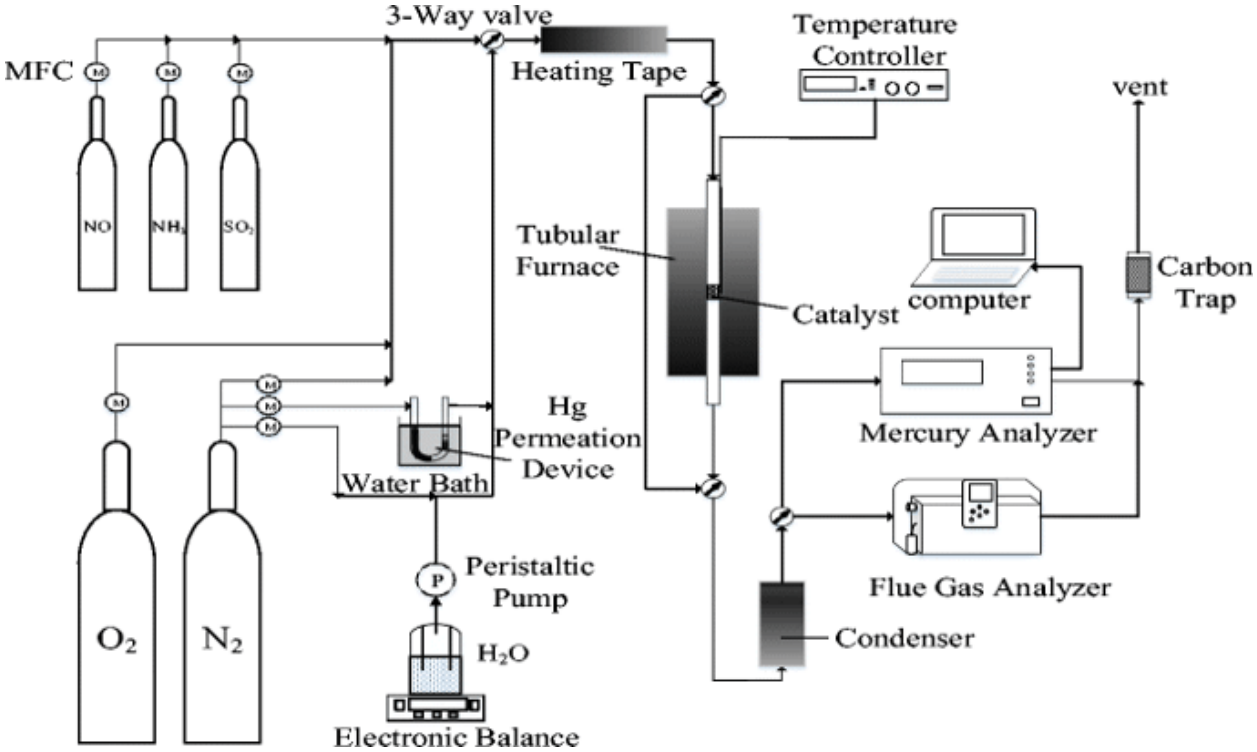

Figure 1. Schematic diagram of the experimental setup

A catalyst sample was loaded in the quartz reactor in each test. The ability of the catalyst to remove NO and Hg^0 was investigated at a temperature from 100 to 300 °C under 40,000 h^{-1} gas hourly space velocity. The total flow rate of the simulated flue gas passing through the fixed-bed reactor was kept at 933 mL/min, including 10% O_2, 1000 ppm NO (when used), 1000 ppm NH_3 (when used), 1000 ppm SO_2 (when used), 5 vol% H_2O (when used), and N_2 as the balance gas. The inlet Hg^0 concentration was approximately 42 μg/m^3. The flow rates of simulated flue gas compositions were accurately controlled by a mass flow controller (MFC). Note that NO changed into NO_2 during the test, so NO_x was used to value the efficiency of NO conversion. The NO_x and Hg^0 concentrations at the inlet and outlet of the reactor were metered by a flue gas analyzer (Nova plus RCU, MRU, Neckarsulm, Germany) and an online mercury analyzer (VM-3000, Mercury Instruments, Karlsfeld, Germany), respectively. Each sampling test and analysis

was performed three times to reduce the error and uncertainty. The NO reduction efficiency (E_{NO}) and Hg^0 oxidation efficiency (E_{Hg}) were calculated from the difference in NO_x and Hg^0 concentrations between the inlet and outlet as Eqs. (1) and (2):

$$\mathrm{E_{NO}}(\%) = \frac{NO_{\chi in} - NO_{\chi out}}{NO_{\chi in}} \times 100\% \quad (1)$$

$$\mathrm{E_{Hg}}(\%) = \frac{Hg^0_{in} - Hg^0_{out}}{Hg^0_{in}} \times 100\% \quad (2)$$

where NO_{xin} and Hg^0_{in} were the concentrations of NO_x and Hg^0 at the inlet of the reactor, and NO_{xout} and Hg^0_{in} were the concentrations of NO_x and Hg^0 at the outlet of the reactor, respectively.

Results and discussion

Performance of $Ce_xZr_yMn_zO_2$ catalysts

Simultaneous Hg^0 oxidation and NO conversion. The prepared $Ce_xZr_yMn_zO_2$ catalysts were first used to simultaneously remove NO and Hg^0 in a SCR atmosphere at a temperature from 100 to 300 °C, and the results are shown in Fig. 2.

As shown in Fig. 2a, the simultaneous efficiency of NO conversion in the SCR atmosphere first increased and then decreased when the temperature rose. The catalysts had the highest efficiency of NO conversion around 150 to 200 °C. In Fig. 2b, the simultaneous efficiency of Hg^0 oxidation remained higher than 90% from 100 to 300 °C, although the catalysts had different molar ratios of Ce, Zr, and Mn. This indicates that all the catalysts provided good Hg^0 oxidation at low temperature.

The $Ce_{0.12}Zr_{0.17}Mn_{0.71}O_2$, $Ce_{0.23}Zr_{0.32}Mn_{0.45}O_2$, and $Ce_{0.47}Zr_{0.22}Mn_{0.31}O_2$ catalysts reached the highest simultaneous efficiencies of NO conversion at 200 °C. However, $Ce_{0.23}Zr_{0.32}Mn_{0.45}O_2$ and $Ce_{0.12}Zr_{0.17}Mn_{0.71}O_2$ performed worse in NO conversion than $Ce_{0.47}Zr_{0.22}Mn_{0.31}O_2$ below 150 °C. It was obvious that $Ce_{0.47}Zr_{0.22}Mn_{0.31}O_2$ had the best performance in NO conversion among the five catalysts at low temperature. As for simultaneous efficiencies of Hg^0 oxidation, $Ce_{0.16}Zr_{0.22}Mn_{0.62}O_2$ and $Ce_{0.47}Zr_{0.22}Mn_{0.31}O_2$ both showed good Hg^0 oxidation efficiency from 100 to 250 °C compared to the others. The only difference was that the Hg^0 oxidation efficiency of $Ce_{0.16}Zr_{0.22}Mn_{0.62}O_2$ at 100 °C was approximately 1% lower than that of $Ce_{0.47}Zr_{0.22}Mn_{0.31}O_2$. The simultaneous efficiencies of Hg^0 oxidation over $Ce_{0.47}Zr_{0.22}Mn_{0.31}O_2$ remained at 100% below 250 °C. It indicated that $Ce_{0.47}Zr_{0.22}Mn_{0.31}O_2$ performed high activity and stability in Hg^0 oxidation at low temperature. Therefore, the $Ce_{0.47}Zr_{0.22}Mn_{0.31}O_2$ nanocomposite had excellent performance in simultaneous Hg^0 oxidation and NO conversion.

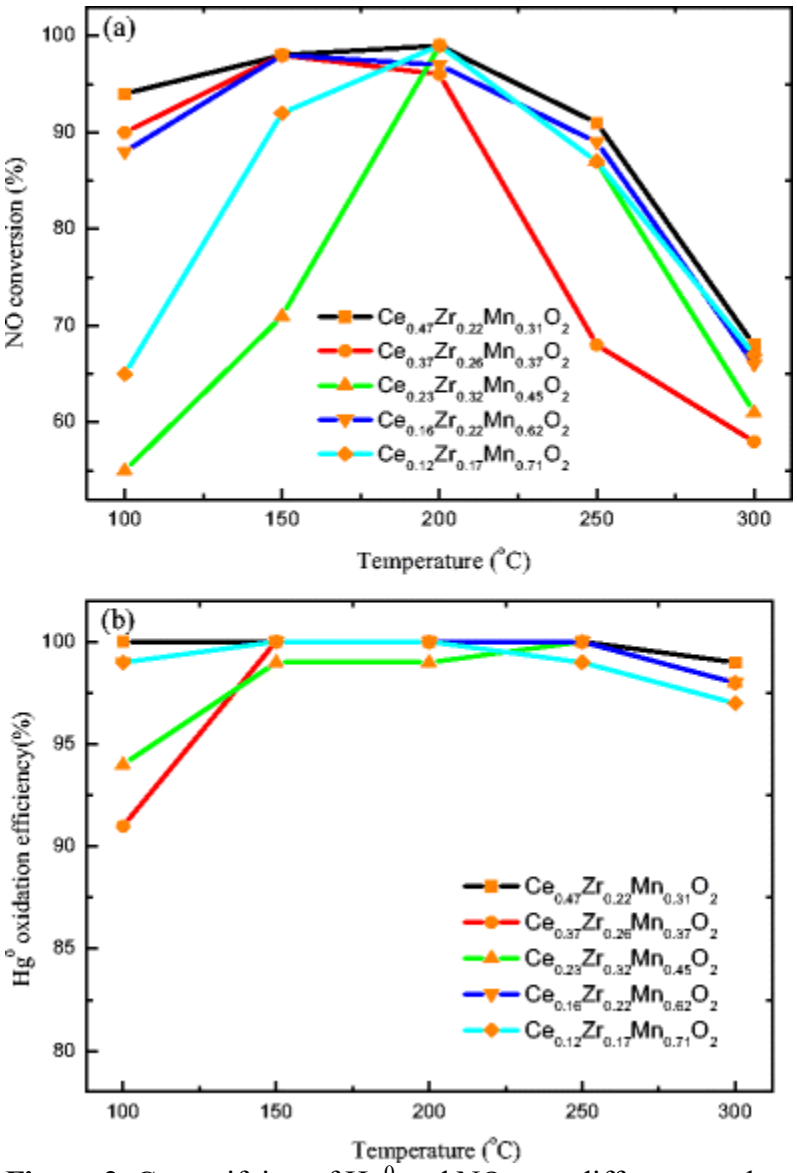

Figure 2. Co-purifying of Hg^0 and NO over different catalysts in simulated flue gas (NH_3/NO = 1): the simultaneous efficiency of **a** NO conversion and **b** Hg^0 oxidation (reaction conditions 42.0 μg/m^3 Hg^0, 1000 ppm NO, NH_3/NO: 1, 10% O_2, gas hourly space velocity 40,000 h^{-1})

As shown in Fig. 2a, the simultaneous efficiency of NO conversion in the SCR atmosphere first increased and then decreased when the temperature rose. The catalysts had the highest efficiency of NO conversion around 150 to 200 °C. In Fig. 2b, the simultaneous efficiency of Hg^0 oxidation remained higher than 90% from 100 to 300 °C, although the catalysts had different molar ratios of Ce, Zr, and Mn. This indicates that all the catalysts provided good Hg^0 oxidation at low temperature.

The $Ce_{0.12}Zr_{0.17}Mn_{0.71}O_2$, $Ce_{0.23}Zr_{0.32}Mn_{0.45}O_2$, and $Ce_{0.47}Zr_{0.22}Mn_{0.31}O_2$ catalysts reached the highest simultaneous efficiencies of NO conversion at 200 °C. However, $Ce_{0.23}Zr_{0.32}Mn_{0.45}O_2$ and $Ce_{0.12}Zr_{0.17}Mn_{0.71}O_2$ performed worse in NO conversion than

$Ce_{0.47}Zr_{0.22}Mn_{0.31}O_2$ below 150 °C. It was obvious that $Ce_{0.47}Zr_{0.22}Mn_{0.31}O_2$ had the best performance in NO conversion among the five catalysts at low temperature. As for simultaneous efficiencies of Hg^0 oxidation, $Ce_{0.16}Zr_{0.22}Mn_{0.62}O_2$ and $Ce_{0.47}Zr_{0.22}Mn_{0.31}O_2$ both showed good Hg^0 oxidation efficiency from 100 to 250 °C compared to the others. The only difference was that the Hg^0 oxidation efficiency of $Ce_{0.16}Zr_{0.22}Mn_{0.62}O_2$ at 100 °C was approximately 1% lower than that of $Ce_{0.47}Zr_{0.22}Mn_{0.31}O_2$. The simultaneous efficiencies of Hg^0 oxidation over $Ce_{0.47}Zr_{0.22}Mn_{0.31}O_2$ remained at 100% below 250 °C. It indicated that $Ce_{0.47}Zr_{0.22}Mn_{0.31}O_2$ performed high activity and stability in Hg^0 oxidation at low temperature. Therefore, the $Ce_{0.47}Zr_{0.22}Mn_{0.31}O_2$ nanocomposite had excellent performance in simultaneous Hg^0 oxidation and NO conversion.

A long-duration test was further performed at 200 °C to investigate the performance of $Ce_{0.47}Zr_{0.22}Mn_{0.31}O_2$, and the results are shown in Fig. 3.

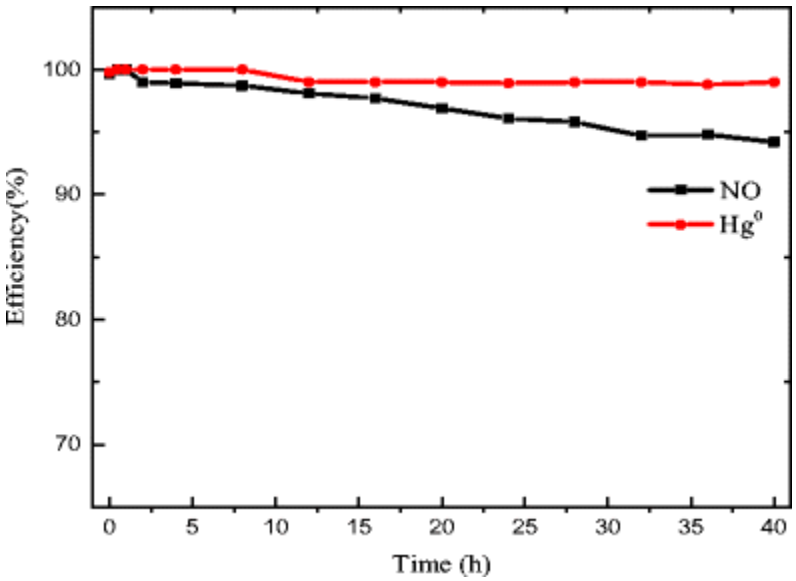

Figure 3. Effect of time on the simultaneous removal of Hg^0 and NO over $Ce_{0.47}Zr_{0.22}Mn_{0.31}O_2$ at 200 °C (reaction conditions 42.0 μg/m^3 Hg^0, 1000 ppm NO, NH_3/NO: 1, 10% O_2, gas hourly space velocity 40,000 h^{-1})

The simultaneous efficiencies of NO conversion and Hg^0 oxidation progressively reduced as time went on, especially for NO conversion efficiency. The simultaneous efficiency of NO conversion decreased from 100 to 94% after 40 h. Hg^0 oxidation efficiency slightly decreased from 100 to 99%, remaining high through 40 h. These results indicate that the $Ce_{0.47}Zr_{0.22}Mn_{0.31}O_2$ had high simultaneous efficiencies of NO conversion and Hg^0 oxidation for a long duration.

Effect of H_2O and SO_2 on simultaneous Hg^0 oxidation and NO conversion. In real applications, water vapor and SO_2 are inevitable in the combustion exhaust. The effects of H_2O and SO_2 on the simultaneous removal of Hg^0 and NO over the $Ce_{0.47}Zr_{0.22}Mn_{0.31}O_2$ catalyst at 200 °C were tested. The results are shown in Fig. 4.

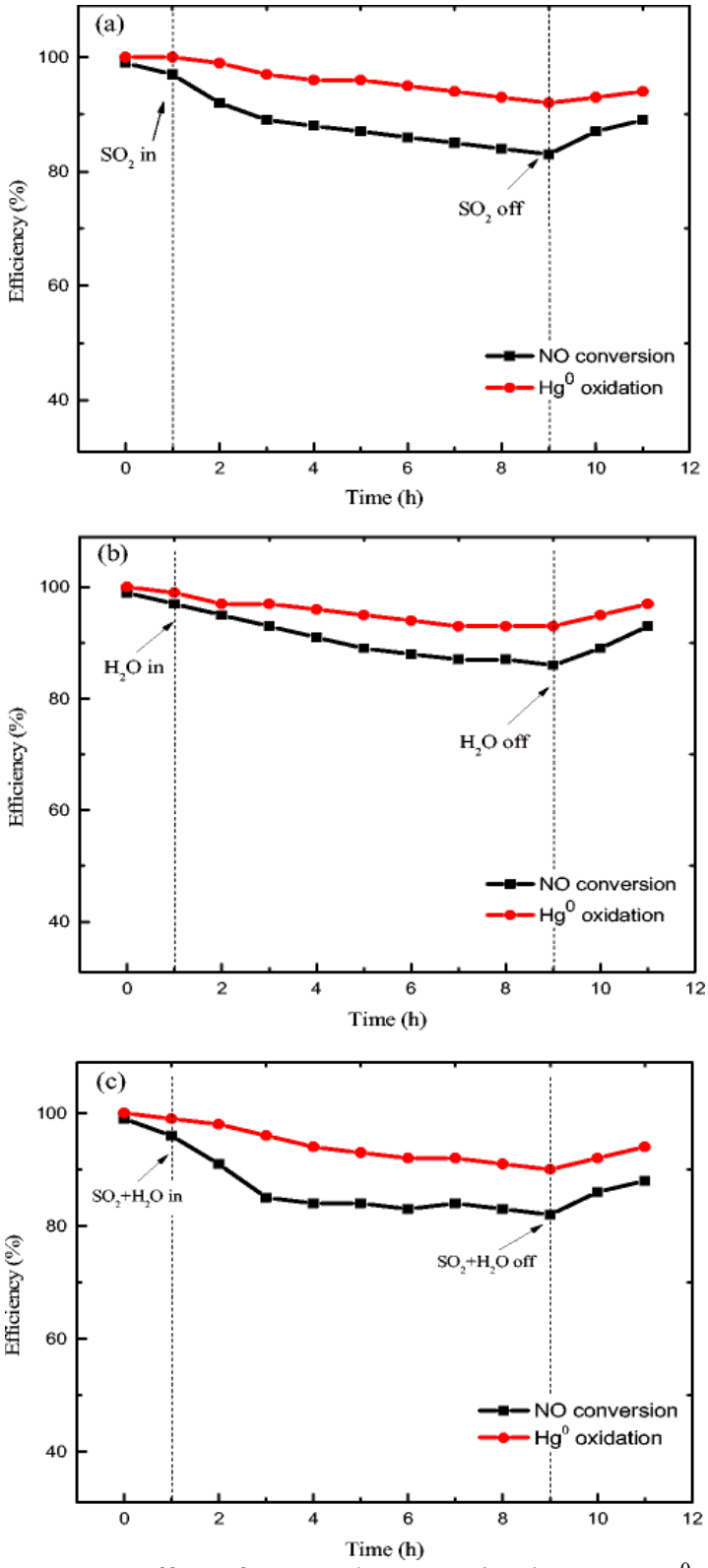

Figure 4. Effect of H_2O and SO_2 on simultaneous Hg^0 oxidation and NO conversion over $Ce_{0.47}Zr_{0.22}Mn_{0.31}O_2$ at 200 °C: **a** the effect of SO_2, **b** the effect of H_2O, and **c** the effect of H_2O and SO_2 (reaction conditions 42.0 μg/m^3 Hg^0, 1000 ppm NO, NH_3/NO: 1, 10% O_2, 1000 ppm SO_2 [when used], 5 vol% H_2O [when used], gas hourly space velocity 40,000 h^{-1})

From Fig. 4a, the addition of 1000 ppm SO_2 had negative effects on both Hg^0 oxidation and NO conversion. The efficiency of Hg^0 oxidation dropped from 100 to 92% after 8 h of SO_2, and the efficiency of NO conversion dropped from 99 to 83%. After removing SO_2, the two efficiencies returned to higher levels, but less than the original values. The inhibition by SO_2 was possibly due to the formation of ammonium sulfate, which would cover the active surface sites and influence the catalytic activity, and the competitive adsorption of SO_2 and Hg^0/NO (Liu et al. 2017; Reddy et al. 2015; Zhang et al. 2015a).

As shown in Fig. 4b, the addition of 5 vol% H_2O also had adverse effects on the simultaneous removal of Hg^0 and NO. When 5 vol% H_2O was added in the simulated flue gas, the efficiency of Hg^0 oxidation decreased. Correspondingly, the efficiency of NO conversion decreased from 99 to 86%. It was probably due to the competitive adsorption between H_2O and NH_3 for the reaction sites (Ding et al. 2015; Qu et al. 2013a). When H_2O was cut off from the flue gas, the removal efficiencies of NO and Hg^0 could be remarkably enhanced.

Figure 4c shows its catalytic performance with both SO_2 and H_2O components together. Hg^0 oxidation efficiency decreased from 100 to 90%, while NO conversion efficiency decreased from 99 to 82% after 8 h treatment of SO_2 and H_2O. After SO_2 and H_2O were simultaneously cut off, both Hg^0 oxidation efficiency and NO conversion efficiency were partially restored. It suggested that $Ce_{0.47}Zr_{0.22}Mn_{0.31}O_2$ exhibited good resistance to SO_2 and H_2O poisoning at 200 °C.

Effect of Hg^0 on NO conversion. The NO conversion efficiency of the $Ce_{0.47}Zr_{0.22}Mn_{0.31}O_2$ under different Hg^0 concentrations is shown in Fig. 5.

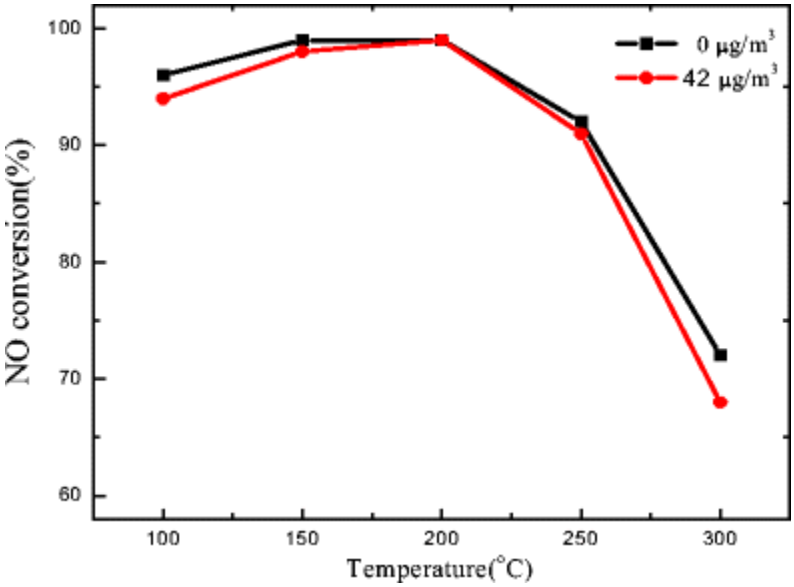

Figure 5. Effect of Hg^0 oxidation on NH_3-SCR of NO over $Ce_{0.47}Zr_{0.22}Mn_{0.31}O_2$

The NO conversion efficiency without Hg^0 was a bit higher than that with 42 μg/m^3 Hg^0. However, the NO conversion efficiency with 42 μg/m^3 Hg^0 was the same as that without Hg^0 at 200 °C. With increasing temperature, the two NO conversion efficiencies both increased at first

and then decreased. In addition, the gap between the two efficiencies narrowed from 100 to 200 °C and broadened from 200 to 300 °C. This indicates that the addition of 42 μg/m^3 Hg^0 had only a small adverse effect on the NO conversion by the $Ce_{0.47}Zr_{0.22}Mn_{0.31}O_2$ at low temperature. In NH_3-SCR reaction, NH_3 is firstly adsorbed on the $Ce_{0.47}Zr_{0.22}Mn_{0.31}O_2$ catalyst and then had an effect on the NO conversion (Zhang et al. 2017a). With the addition of Hg^0, the competitive adsorption between Hg^0 and NH_3 might be the main cause of the lower NO conversion efficiency.

Effect of SCR gas on Hg^0 oxidation. The main intent of this work was to investigate the function of $Ce_xZr_yMn_zO_2$ catalysts in the simultaneous removal of Hg^0 and NO in simulated flue gas. In practical applications, SCR gas is indispensable in NO conversion. The effect of SCR gas on Hg^0 oxidation by the $Ce_{0.47}Zr_{0.22}Mn_{0.31}O_2$ catalyst is shown in Fig. 6.

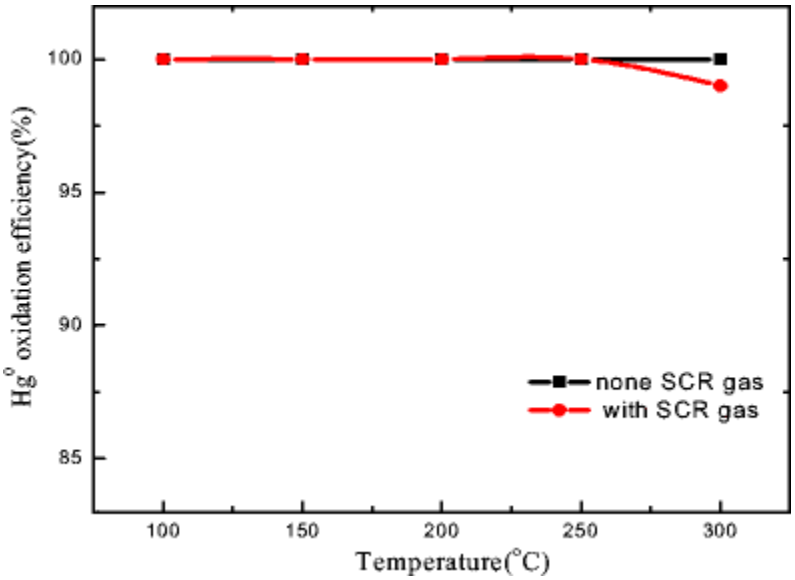

Figure 6. Effect of NH_3-SCR of NO on Hg^0 oxidation over $Ce_{0.47}Zr_{0.22}Mn_{0.31}O_2$ (with SCR gas: 42.0 μg/m^3 Hg^0, 1000 ppm NO, 1000 ppm NH_3, 10% O_2; or no SCR gas: 42.0 μg/m^3 Hg^0, 10% O_2; gas hourly space velocity 40,000 h^{-1})

The efficiency of Hg^0 oxidation remained high from 100 to 300 °C in both treatments (in the presence/absence of SCR gas). The only difference was that the efficiency of Hg^0 oxidation with SCR gas was 99% at 300 °C, which was only 1% lower than that without SCR gas. Therefore, the SCR gas in the test had little impact on the Hg^0 oxidation by the $Ce_{0.47}Zr_{0.22}Mn_{0.31}O_2$ at low temperature.

Characterization of the catalysts

BET. Table 1 lists the BET surface area, pore volume, and average pore size of the catalysts. The BET surface areas of the catalysts ranged from 95.06 to 119.73 m^2/g. In particular, $Ce_{0.37}Zr_{0.26}Mn_{0.37}O_2$ had the largest BET surface area of 119.73 m^2/g among the five catalysts, and its pore volume of 0.32 cm^3/g and average pore size of 9.35 nm were also the largest. However, the BET surface area of $Ce_{0.47}Zr_{0.22}Mn_{0.31}O_2$, which had the best catalytic performance, was only 96.23 m^2/g. This might be attributed to the synergistic effects of Ce, Zr,

and Mn oxide species, which probably influenced the catalytic performance much more significantly than the specific surface area (SSA), although higher SSA could provide more surface active sites (Reddy et al. 2015; Ozkan et al. 1994).

Table 1. Surface structure properties of $Ce_xZr_yMn_zO_2$ catalysts

Catalyst	BET surface area (m^2/g)	Pore volume (cm^3/g)	Average pore size (nm)
$Ce_{0.12}Zr_{0.17}Mn_{0.71}O_2$	105.93	0.22	7.61
$Ce_{0.16}Zr_{0.22}Mn_{0.62}O_2$	95.06	0.19	7.66
$Ce_{0.23}Zr_{0.32}Mn_{0.45}O_2$	113.49	0.26	8.29
$Ce_{0.37}Zr_{0.26}Mn_{0.37}O_2$	119.73	0.32	9.35
$Ce_{0.47}Zr_{0.22}Mn_{0.31}O_2$	96.23	0.20	7.81

TEM. Figure 7 shows the TEM images of the $Ce_{0.47}Zr_{0.22}Mn_{0.31}O_2$ catalyst at 200-, 100-, 20-, and 10-nm resolution. Many crystal grains with similar tiny size combined together, forming the CeO_2-ZrO_2-MnO_2 solid solution. The average diameter of the catalyst was around 8 nm. It indicated that the diameter of the catalyst reached the nanometer grade, which could contribute to the high catalytic performance by providing more surface active sites (Zhang et al. 2017a). This finding is consistent with the BET results, which suggested that the porous structure and small particle size of $Ce_{0.47}Zr_{0.22}Mn_{0.31}O_2$ were beneficial for gaseous reaction (Ma et al. 2017).

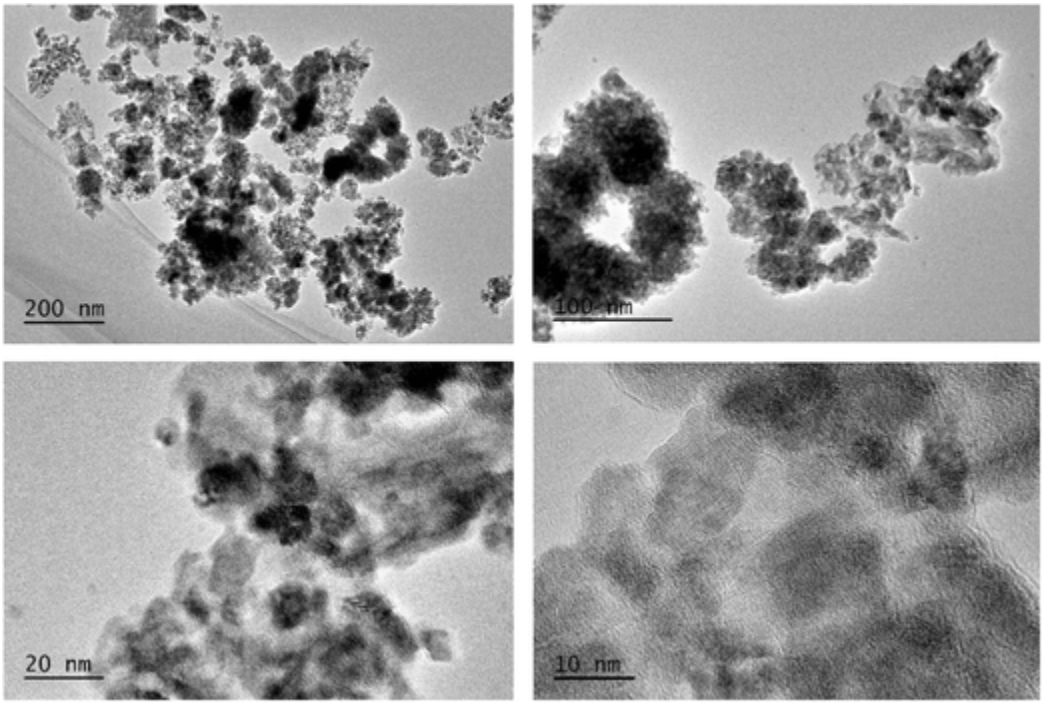

Figure 7. Transmission electron microscopy images of the $Ce_{0.47}Zr_{0.22}Mn_{0.31}O_2$ catalyst

XRD. The powder XRD patterns of $Ce_xZr_yMn_zO_2$ catalysts with different components are shown in Fig. 8.

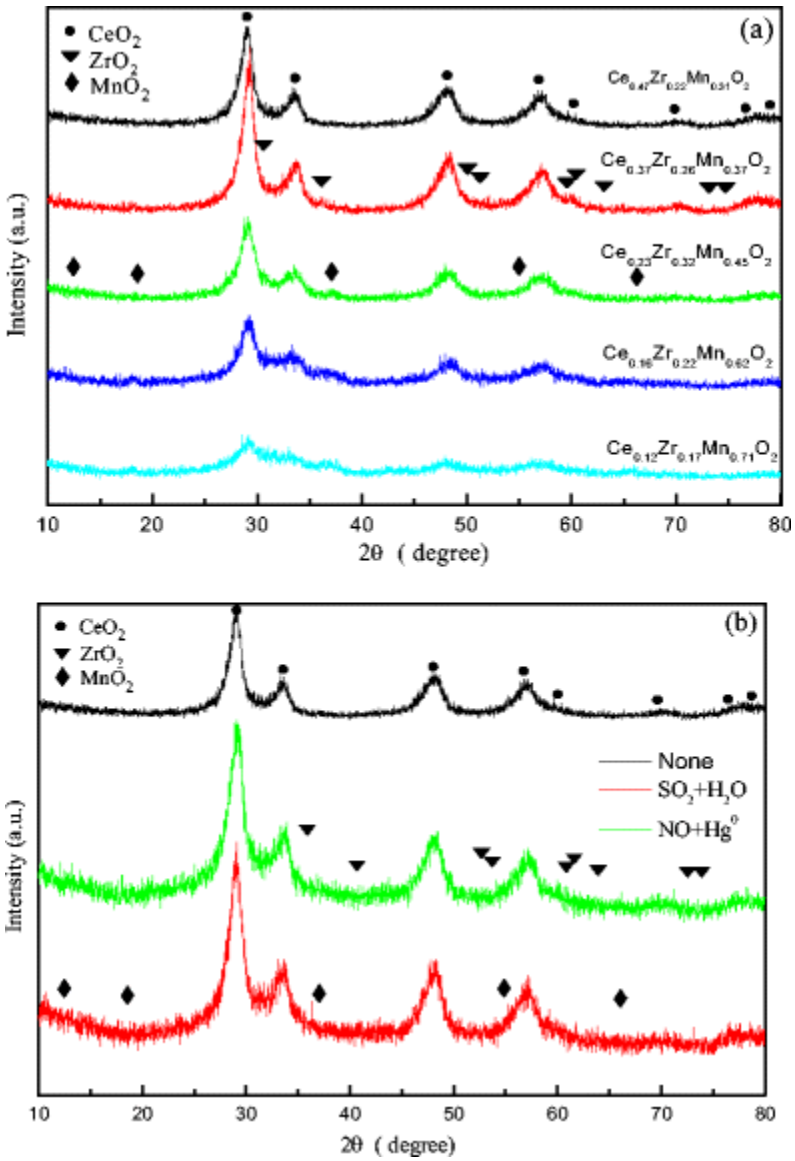

Figure 8. X-ray diffraction patterns: **a** Ce-Zr-MnO_2 catalysts, **b** fresh $Ce_{0.47}Zr_{0.22}Mn_{0.31}O_2$ (none) and used catalyst after the test with $H_2O + SO_2$ or without H_2O and SO_2 ($NO + Hg^0$)

As illustrated in Fig. 8a, all peaks are indexed and referred with the Powder Diffraction Files (PDF). The diffraction peaks at 28.6°, 33.2°, 47.9°, 56.8°, 59.6°, 69.5°, 76.7°, and 79.1° correspond to the (111), (200), (220), (311), (222), (400), (331), and (420) crystal planes of CeO_2 (PDF# 01-0800). The diffraction peaks at 30.4°, 35.5°, 50.3°, 50.9°, 59.6°, 60.4°, 63.1°, 73.3°, and 74.6° could be indexed to the respective crystal planes (111), (200), (202), (220), (113), (311), (222), (004), and (400) of ZrO_2 (PDF# 02-0733). The diffraction peaks at 12.2°, 18.6°, 36.8°, 54.9°, and 65.7° correspond to the respective crystal planes (110), (200), (211), (431), and (112) of MnO_2 (PDF# 18-0802). When the proportion of cerium in the $Ce_x Zr_y Mn_z O_2$ catalyst increased, the diffraction peaks of CeO_2 became more obvious, which might be due to the better crystallization of cerium oxide (Reddy et al. 2005). The characteristic peaks of ZrO_2 and MnO_2 were inconspicuous, indicating that the impregnated ZrO_2 and MnO_2 were in a highly dispersed or amorphous state in the solid solution (Zhang et al. 2015c).

Crystalline metal oxide species, like CeO_2, would provide more active sites for catalytic reactions than amorphous materials with structure distortion properties, which was ascribed from that increased CeO_2 proportion resulted in increased catalytic activity (Reddy et al. 2005).

Figure 8b shows the powder XRD patterns of the fresh $Ce_{0.47}Zr_{0.22}Mn_{0.31}O_2$ catalyst, the one after the simultaneous Hg^0 oxidation and NO conversion test, and the one tested with the presence of H_2O and SO_2, respectively. The three patterns are substantially the same, which indicates that there is no obvious difference in the crystal structures between before and after used samples. In other words, the catalyst remained stable during the simultaneous Hg^0 oxidation and NO conversion test, even with the effects of H_2O and SO_2.

XPS. To further investigate the chemical states of the elements on the catalysts' surface, the catalysts were characterized by XPS. The surface atomic characteristics of Ce, Zr, Mn, and O were measured and are shown in Fig. 9.

As shown in Fig. 9(a1) to (e1), the O 1s XPS spectra of the fresh Ce-Zr-Mn-O_2 catalysts were all divided into two peaks. The peaks around 529.3–529.5 eV can be regarded as the lattice oxygen (O_β), and the binding energy peaks around 531.1–532.0 eV are attributed to chemisorbed oxygen (O_α) (Zhang et al. 2017a; Chi et al. 2017). The effect of oxygen on activity and selectivity is noteworthy in both SCR and ammonia oxidation reactions (Ettireddy et al. 2012). It has been shown that O_α can be regarded as the most active oxygen, which benefits the reactive oxidation process (Song et al. 2016; Yang et al. 2006). O_β, as the lattice oxygen species, can easily bond with adsorbed mercury to form HgO in the adsorption and oxidation reaction of Hg^0 over the surface of catalysts (Zhang et al. 2015c; Yang et al. 2015). It can also be stored and released by ceria via the redox shift between Ce^{4+} and Ce^{3+} (Bin et al. 2014). This situation could generate additional chemisorbed oxygen on the surface of the catalyst, which might affect the redox properties and nitrogen oxide/ammonia adsorption capacity of the catalysts (Liu et al. 2013). Among the five catalysts, the $O_\alpha/(O_\alpha + O_\beta)$ ratios were different, but they all had good performance in the simultaneous removal of NO and Hg^0. After the simultaneous removal of NO and Hg^0 test, shown in Fig. 9(f1), both O_α and O_β decreased. This indicates that, with the existence of ceria, the lattice oxygen can be changed into chemisorbed oxygen and benefit the redox properties. The importance of ceria was also supported by the finding that $Ce_{0.47}Zr_{0.22}Mn_{0.31}O_2$ performed best, although it had the lowest $O_\alpha/(O_\alpha + O_\beta)$ ratio. Moreover, this illustrates the synergistic effects of cerium and manganese to promote catalytic activity.

Figure 9(e2) and (f2) shows the Ce 3d XPS spectra of fresh and used $Ce_{0.47}Zr_{0.22}Mn_{0.31}O_2$, respectively. *u* and *v* refer to the $3d_{5/2}$ and $3d_{7/2}$ spin-orbit components, respectively (Mullins et al. 1998). The peaks labeled u_1 and v_1 are assigned to Ce^{3+}, while the peaks denoted *u*, u_2, u_3, *v*, v_2, and v_3 represent Ce^{4+} (Fang et al. 2007; Gao et al. 2010). All of the catalysts exhibited a total of eight peaks attributed to the Ce^{4+} and Ce^{3+} oxidation states, while the ratio of $Ce^{3+}/(Ce^{3+} + Ce^{4+})$ increased from 15 to 20% after use. This indicates that Ce^{4+} was the main form of cerium on the surface. In addition, Ce^{4+} was reduced to Ce^{3+} during the test, coincident with the decrease of the $O_\alpha/(O_\alpha + O_\beta)$ ratio shown in Fig. 9(f1) according to the reaction $2CeO_2 \leftrightarrow Ce_2O_3 + O_\beta$. However, the ratio of $Ce^{3+}/(Ce^{3+} + Ce^{4+})$ did not significantly increase, perhaps because the Ce^{3+} was oxidized into Ce^{4+} again by the redox equilibrium.

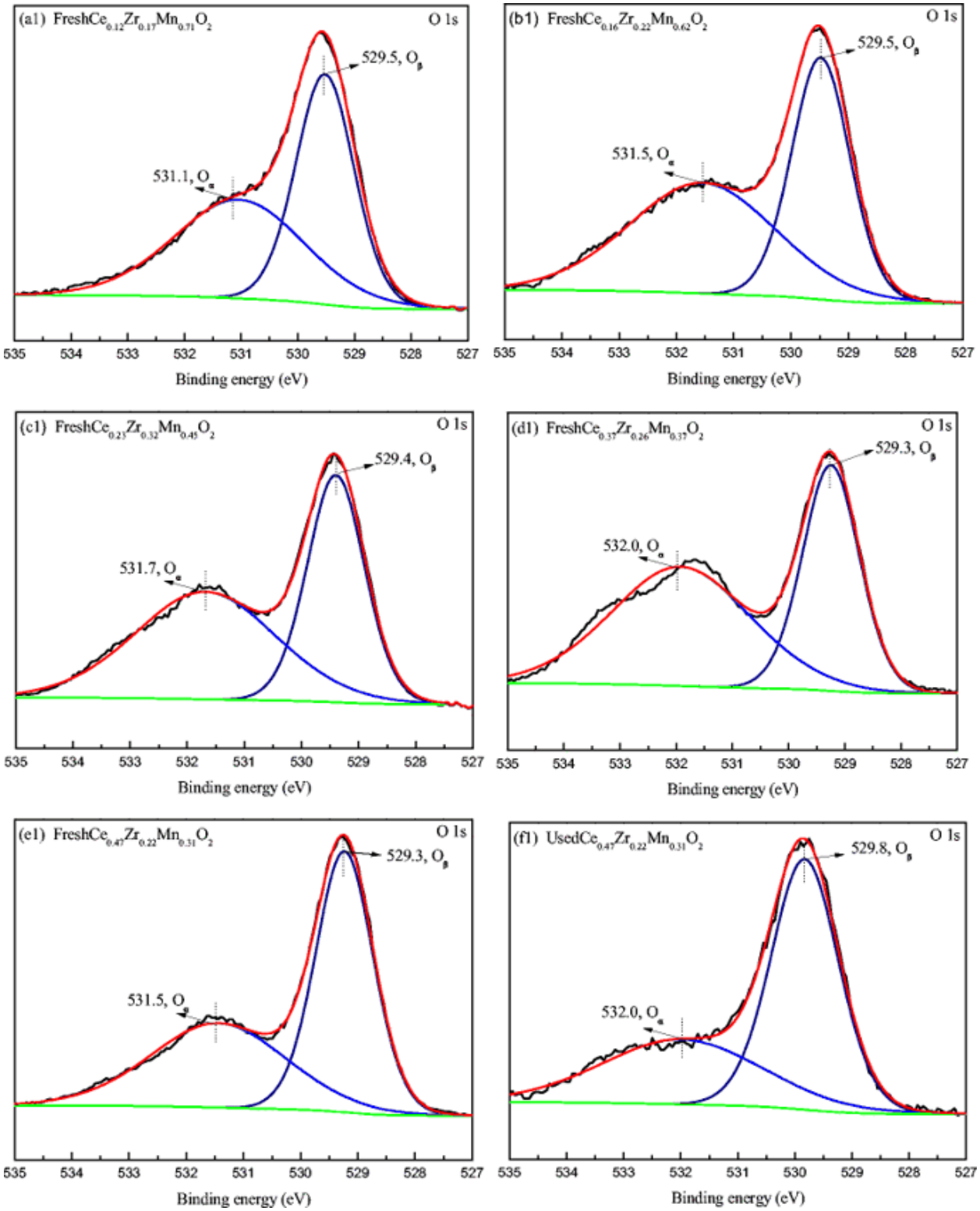

Figure 9. X-ray photoelectron spectroscopy spectra of the fresh or used catalysts over the spectral regions of Ce 3d, Zr 3d, Mn 2p, and O 1s

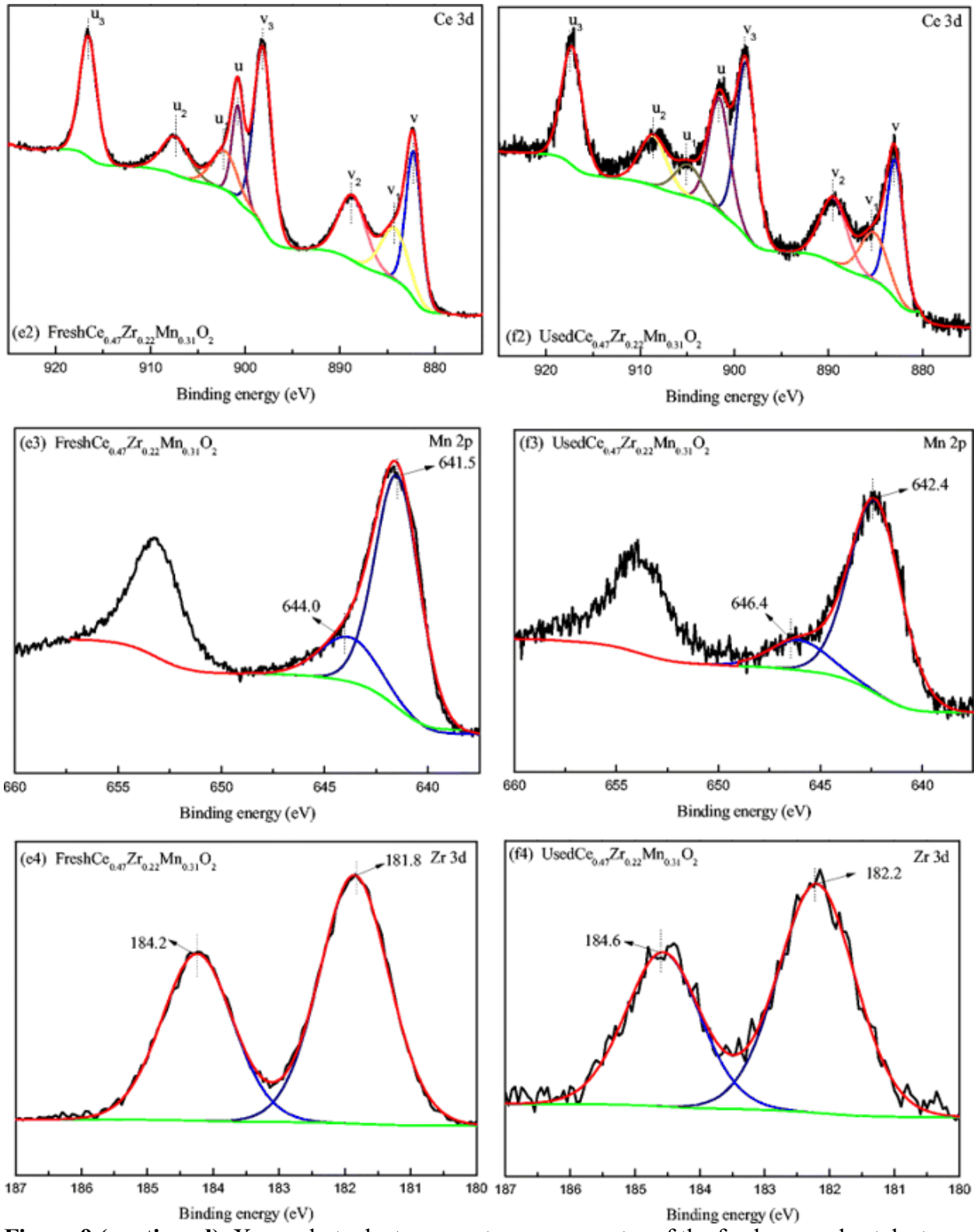

Figure 9 (continued). X-ray photoelectron spectroscopy spectra of the fresh or used catalysts over the spectral regions of Ce 3d, Zr 3d, Mn 2p, and O 1s

As shown in Fig. 9(e3), for Mn 2p of fresh $Ce_{0.47}Zr_{0.22}Mn_{0.31}O_2$, the two characteristic peaks at 644.0 and 641.5 eV correspond to the valences of Mn^{4+} and Mn^{3+}, respectively (He et al. 2014; Pappas et al. 2016); no Mn^{2+} peak was observed. Figure 9(f3) shows that the atomic ratio of $Mn^{4+}/(Mn^{3+} + Mn^{4+})$ in the used catalyst was 15%, while the ratio was 21% in the fresh one. This illustrates that the Mn^{4+} changed into Mn^{3+} during the test, which also indicates that electron transfer occurred, accompanied by the formation of oxygen vacancies. The reduction of Mn^{4+} to Mn^{3+} resulted from the Mn^{4+} adsorbed electrons in oxygen vacancies to form Mn^{3+} ($Mn^{4+} + e^- \rightarrow Mn^{3+}$), which probably contributed to the oxidation of NO and Hg^0 (Wang et al. 2015; Boningari et al. 2015). Hence, the oxygen defect formation at MnO_2 surfaces might play a key role in its catalytic activity due to the low oxygen vacancy formation energy providing a favorable thermodynamic pathway for catalytic processes, such as 0.97 eV for (110), 1.09 eV for (211), and 0.07 eV for (112) (Tompsett et al. 2014).

The Zr 3d binding energies of the fresh $Ce_{0.47}Zr_{0.22}Mn_{0.31}O_2$ are shown in Fig. 9(e4). The Zr 3d spectra show two peaks, corresponding to Zr $3d_{3/2}$ at 184.2 eV and Zr $3d_{5/2}$ at 181.8 eV, both of which are assigned to Zr^{4+} (Picasso et al. 2007; Younes et al. 2003). After the test, the Zr 3d of used $Ce_{0.47}Zr_{0.22}Mn_{0.31}O_2$, as shown in Fig. 9(f4), showed no difference as compared with the fresh one, except for a shift of both peaks to higher binding energy values. All four elements' peaks shifted to the higher binding energy values after the test, which might be associated with more electron-attractive species adsorbed on the surface of the catalyst after the test (Xie et al. 2013; Song et al. 2016).

The XPS results indicate that the redox reactions of Ce and Mn played major roles in the simultaneous removal of NO and Hg^0.

FT-IR. Figure 10 illustrates the FT-IR spectra of the five catalysts. For $Ce_{0.12}Zr_{0.17}Mn_{0.71}O_2$, the band at 3400 cm^{-1} can be attributed to the hydroxyl groups adsorbed on the surface of the catalyst (Ma et al. 2017; Schmitt and Flemming 1998). The band at 2934 cm^{-1} and some weak bands around this wave number are due to the CH_3/CH_2 groups (Schmitt and Flemming 1998; Rivas et al. 2008). The adsorption peak at 1623 cm^{-1} is attributed to the bridging bidentate nitrates (Zhang et al. 2017a; Wang et al. 2017). Moreover, the absorption bands at 1532 cm^{-1} correspond to NO_2-containing species (Zhang et al. 2017a; Zhao et al. 2016a). The bands at 1395 and 1047 cm^{-1} correspond to C–O and O–C–O bending vibrations (Schmitt and Flemming 1998). The appearance of all these bands could account for the adsorption of the H_2O, CO_2, NO_3^-, NH_3, and other carbon-hydrogen compounds present in the air or from the preparation (Padmanathan and Selladurai 2014; Santos et al. 2008). The strong intense band at 560 cm^{-1} is ascribed to the Mn–O, Ce–O, and Zr–O hybrid vibrations (Reddy et al. 2005; Marzouk et al. 2017; Aghazadeha et al. 2016). The adsorption bands of $Ce_{0.23}Zr_{0.32}Mn_{0.45}O_2$ and $Ce_{0.16}Zr_{0.22}Mn_{0.62}O_2$ were analogous, despite small shifting of the peaks. Compared to the three catalysts above, the peaks of $Ce_{0.37}Zr_{0.26}Mn_{0.37}O_2$ and $Ce_{0.47}Zr_{0.22}Mn_{0.31}O_2$ were much more abundant, while the peaks were similar to the others above 1000 cm^{-1}. This difference could be attributed to the different vibrations of Mn–O, Ce–O, and Zr–O. These results illustrate that the metallic oxides were well dispersed on the surface of the catalysts, contributing to a high catalytic activity (Li et al. 2015). Therefore, the large amount of active groups adsorbed on the surface of the catalysts benefited the removal of NO and Hg^0.

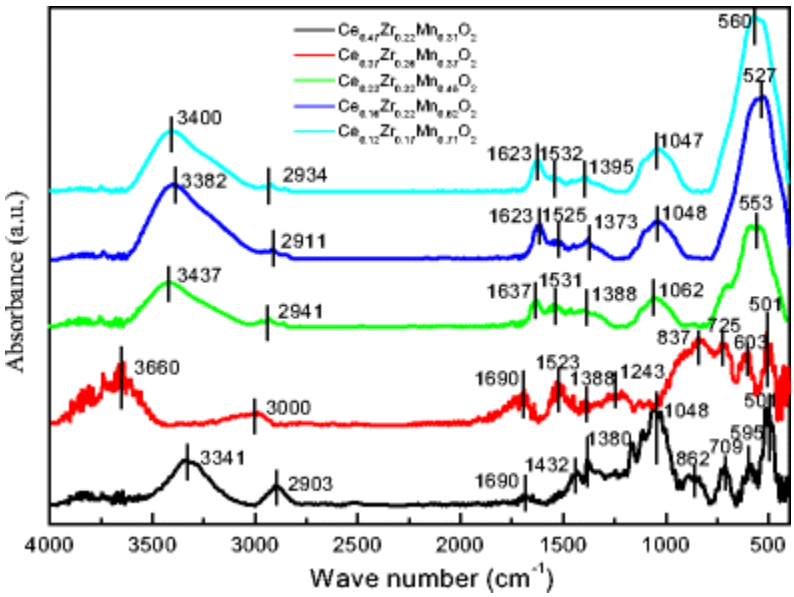

Figure 10. Fourier transform infrared spectra of the five catalysts

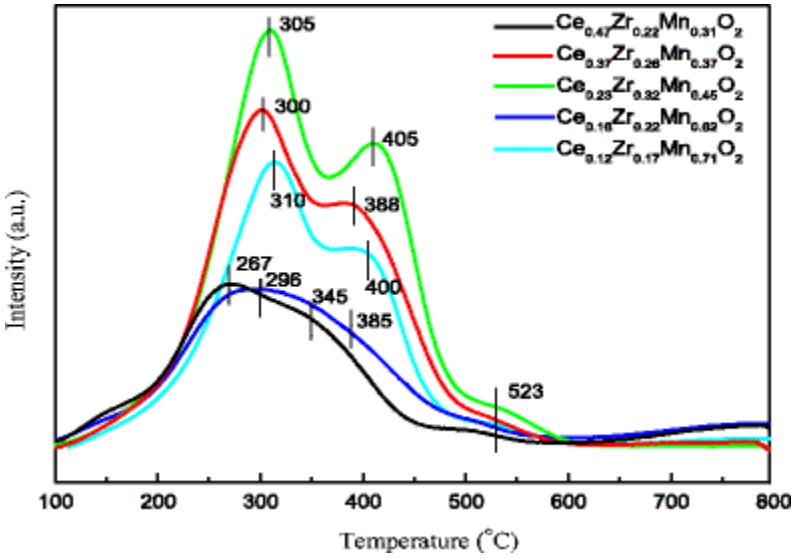

Figure 11. Temperature-programmed reduction of H_2 properties of the five catalysts

H_2-TPR. The redox properties of the catalysts, which were obtained by H_2-TPR, are shown in Fig. 11.

The $Ce_{0.23}Zr_{0.32}Mn_{0.45}O_2$ shows three peaks at 305, 405, and 523 °C, respectively. The peak at 305 °C was the strongest, which could be attributed to the reduction of Mn^{4+} to Mn^{3+}. In addition, the peak at 405 °C could correspond to the reduction of Mn^{3+} to Mn^{2+} (Ma et al. 2017; Xu et al. 2015). This agrees with the results from XPS showing that only Mn^{4+} and Mn^{3+} existed, whether the catalyst was used or not, as the test temperature was only 200 °C, which was much lower than the reduction temperature of Mn^{3+} to Mn^{2+}. The weakest peak at 523 °C could be interpreted as the reduction of Ce^{4+} to Ce^{3+} (Chi et al. 2017; Zhu et al. 2004). As for the remaining four catalysts, the three characteristic peaks could also be observed. For the catalysts of $Ce_{0.16}Zr_{0.22}Mn_{0.62}O_2$ and $Ce_{0.47}Zr_{0.22}Mn_{0.31}O_2$, the peaks were not obvious, indicating that the

overlap reduction of surface Mn^{4+} to Mn^{3+} and Ce^{4+} to Ce^{3+} presents due to the interaction between Mn and Ce oxides, which could highly support the strong synergetic effect on the mobility of surface oxygen and the activation of lattice oxygen. Combined with the results of the simultaneous removal of NO and Hg^0, the catalysts had high catalytic efficiency of Hg^0 oxidation at low temperature, mainly because of the reduction of Mn^{4+} to Mn^{3+} at low temperature. Moreover, all of the catalysts performed well at Hg^0 oxidation, perhaps because the Hg^0 content was insignificant compared to the manganese content, even given the worst-case reducibility. In addition, the first peak of $Ce_{0.47}Zr_{0.22}Mn_{0.31}O_2$ at 267 °C was the lowest one among the five catalysts, which might have contributed to the best performance of $Ce_{0.47}Zr_{0.22}Mn_{0.31}O_2$ at low temperature.

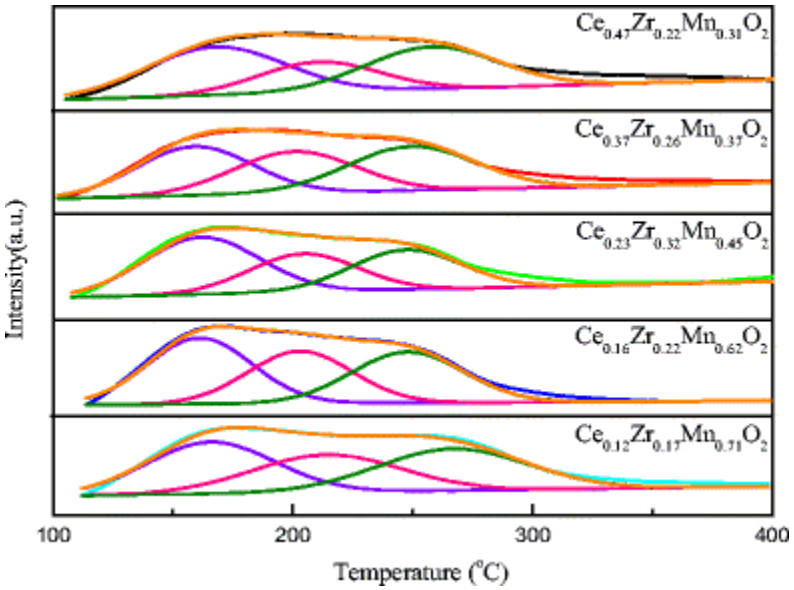

Figure 12. Temperature-programmed desorption of NH_3 properties of the five catalysts

NH_3-TPD. NH_3-TPD was performed to investigate the surface acidities of the $Ce_xZr_yMn_zO_2$ catalysts, and the profiles are shown in Fig. 12.

There were three broad peaks at 159–169, 201–215, and 247–268 °C, indicating the presence of acid sites with different thermal stabilities (Wang et al. 2017). The first peaks at the lowest temperature range (159–169 °C) could be assigned to physically adsorbed NH_3, the peak at 201–215 °C could be assigned to the desorption of NH^{4+} from the strong Brønsted acid sites, and the peak at 247–268 °C was the ammonia strongly adsorbed on the Lewis acid sites (Watanabe et al. 2009; Zhang et al. 2015b). The three broad peaks indicated that there were abundant acid sites on the surface of the $Ce_xZr_yMn_zO_2$ catalysts, which benefited the NO conversion because NH_3 was well adsorbed (Peng et al. 2013; Qu et al. 2013b). Moreover, this result was consistent with the excellent NO removal performance of the catalysts that when the temperature was higher than 200 °C, the NH_3 adsorbed in Brønsted acid sites have desorbed, so the SCR activity became lower.

Interaction and mechanism discussion. For the $Ce_{0.47}Zr_{0.22}Mn_{0.31}O_2$ catalyst, the reactions on the surface included both Hg^0 oxidation (Hg^0 was oxidized to Hg^{2+}) and NO conversion (NO was

reduced by NH_3), which were aided by the synergetic effect on the mobility of surface oxygen and the activation of lattice oxygen. The synergistic mechanism could be described as follows:

$$Mn_2O_3 + 2CeO_2 \leftrightarrow 2MO_2 + Ce_2O_3 \quad (3)$$

$$Ce_2O_3 + \frac{1}{2}O_{2(g)} \rightarrow 2CeO_2 \quad (4)$$

The redox equilibrium ($Mn^{3+} + Ce^{4+} \leftrightarrow Mn^{4+} + Ce^{3+}$) played an important role in promoting Hg^0 oxidation and NO conversion by enhancing the reducibleness of CeO_2 and MnO_2. Cerium could occupy two oxidation states (CeO_2 (Ce^{4+}) ↔ Ce_2O_3 (Ce^{3+})), allowing ceria to accommodate more surface lattice oxygen species. Consequently, the presence of CeO_2 increased the redox properties of $Zr_yMn_zO_2$, since low oxygen vacancy formation energy of MnO_2 provided a favorable thermodynamic pathway for the catalytic reoxidation by gas phase oxygen. In addition, the synergetic effect resulted in a decrease of the energy that required for the electron transfer between Ce and Mn active sites, promoting the adsorption and activation of NH_3 and NO, which could greatly improve the Hg^0 oxidation and NO conversion.

Separately, the SCR reaction of NO by NH_3 on the $Ce_{0.47}Zr_{0.22}Mn_{0.31}O_2$ catalyst most probably took place according to the following steps. Gaseous NH_3 was firstly adsorbed on the $Ce_{0.47}Zr_{0.22}Mn_{0.31}O_2$ catalyst to form coordinated $NH_{3(ad)}$, $-NH_{2(ad)}$, and NH_4^+ since Brønsted acid sites and Lewis acid sites presented on the surface of the catalyst. With NO largely adsorbed on $Ce_{0.47}Zr_{0.22}Mn_{0.31}O_2$ catalyst, the $NO_{(ad)}$ could be oxidized to NO_2, which subsequently coupled with the intermediate species to react with $NO_{(ad)}$ to form N_2 and H_2O. The proposed NH_3-SCR mechanisms could be facilitated as follows:

$$NH_{3(g)} \rightarrow NH_{3(ad)} \quad (5)$$

$$NH_{3(ad)} + O^*_{(ad)} \rightarrow -NH_{2(ad)} + OH_{(ad)} \quad (6)$$

$$NO_{(ad)} + -NH_{2(ad)} \rightarrow NH_2NO_{(ad)} \rightarrow N_{2(g)} + H_2O_{(g)} \quad (7)$$

$$2NO_{(g)} + O_{2(g)} \rightarrow 2NO_{2(ad)} \quad (8)$$

$$NO_{2(ad)} + OH_{(ad)} \rightarrow O_{(ad)} + HNO_{2(ad)} \quad (9)$$

$$HNO_{2(ad)} + NH_{3(ad)} \rightarrow NH_4NO_2 \rightarrow NH_2NO_{(ad)} + H_2O \rightarrow N_{2(g)} + 2H_2O_{(g)} \quad (10)$$

$$NH_{3(g)} \rightarrow NH^+_{4(ad)} \quad (11)$$

$$2NH^+_{4(ad)} + NO_{2(ad)} + NO_{(g)} \rightarrow 2N_{2(g)} + 3H_2O_{(g)} + 2H^+ \quad (12)$$

Meanwhile, based on the results obtained from H_2-TPR and XPS, a likely reaction pathway for Hg^0 oxidation was related to the Mars-Maessen mechanism. Gaseous Hg^0 was firstly adsorbed on the surface of the catalyst to form $Hg^0_{(ad)}$. Then, the lattice and surface oxygen reacts with

adjacently absorbed Hg^0 to form $HgO_{(ad)}$. The adsorbed mercury is present as both Hg^0 and Hg^{2+} on these ceria-based materials (He et al. 2011). Some of $HgO_{(ad)}$ was captured by the catalyst and the rest re-emits to the gas phase. In the presence of O_2, the redox equilibrium induced the reduced Ce_2O_3 and Mn_2O_3 to be converted back to their original states. The possible mechanism for Hg^0 oxidation could be proposed as follows:

$$Hg^0_{(g)} \rightarrow Hg^0_{(ad)} \tag{13}$$

$$Hg^0_{(ad)} + 2CeO_2(MnO_2) \rightarrow HgO_{(ag)} + Ce_2O_3(Mn_2O_3) \tag{14}$$

$$HgO_{(ad)} \rightarrow HgO_{(g)} \tag{15}$$

As for the interaction between NH_3-SCR and Hg^0, it was shown in Figs. 5 and 6 that the NO conversion of $Ce_{0.47}Zr_{0.22}Mn_{0.31}O_2$ could be slightly influenced by Hg^0, while that of Hg^0 could rarely be affected by the selected catalytic reduction process of NO.

It had been illustrated that the Hg^0 oxidation activity could be suppressed by NH_3 in accordance with the following reaction (Chi et al. 2017):

$$3Hg^{2+} + 2NH_3 \rightarrow 3Hg^0 + N_2 + 6H^+ \tag{16}$$

However, the negative effect of NH_3 on Hg^0 oxidation was more obvious at high temperature (> 325 °C) (Chi et al. 2017). It was consistent with the result of the SCR gas effect, shown in Fig. 6, that the efficiency of Hg^0 oxidation was only a bit suppressed at 300 °C.

In addition, the adverse effect of Hg^0 to NO was more notable. In general, Hg^0, NH_3, and NO were firstly adsorbed on the $Ce_{0.47}Zr_{0.22}Mn_{0.31}O_2$ catalyst from the results described above. Therefore, it might be the competitive adsorption between Hg^0 and NH_3 that resulted in the decreasing of NO conversion. Gaseous NH_3 was adsorbed on the $Ce_{0.47}Zr_{0.22}Mn_{0.31}O_2$ catalyst to form coordinated $NH_{3(ad)}$, $-NH_{2(ad)}$, and NH_4^+ with Brønsted acid sites and Lewis acid sites firstly, which played an important role in NO conversion. However, the adsorbed Hg^0/Hg^{2+} occupied the surface active sites of the catalyst, which might abate the formation of $NH_{3(ad)}$, $-NH_{2(ad)}$, and NH_4^+ on acid sites, ultimately leading to the inhibition of NO conversion. The NH_3-TPD result (Fig. 12) showed the presence of acid sites with different thermal stabilities. When the temperature rose to 200 °C, Lewis acid sites were the main active sites, which could strongly adsorb ammonia. At that temperature, Hg^0 showed no influence in NO conversion. When the temperature was higher than 200 °C, the ammonia which adsorbed on the Lewis acid sites desorbs from the sites gradually, and the influence of Hg^0 to NO conversion also increased. The results indicated that the inhibitive effect of the oxidation of Hg^0 on the NH_3-SCR of NO was mainly because that Hg^0/Hg^{+2} would occupy the NH_3 adsorption sites except for the Lewis acid sites.

Conclusions

In this study, series of $Ce_xZr_yMn_zO_2$ nanosized catalysts were prepared for the simultaneous oxidation of Hg^0 and NH_3-SCR of NO at low temperature. $Ce_{0.47}Zr_{0.22}Mn_{0.31}O_2$ exhibited

superior Hg^0 removal efficiency (> 99%) and NO conversion (> 90%) even when the temperature was below 250 °C. The oxidation of Hg^0 could slightly have an impact on the NH_3-SCR of NO, while the effect of NH_3 and NO in the SCR system was negligible to the oxidation of Hg^0. The catalyst also exhibited good SO_2 and H_2O durability during the simultaneous removal of Hg^0 and NO, as the simultaneous efficiencies of NO conversion and Hg^0 oxidation could be partially restored after removal of SO_2 and H_2O. The excellent performance of $Ce_{0.47}Zr_{0.22}Mn_{0.31}O_2$e was mainly due to the stronger synergistic effects of Ce-Zr-Mn, the effective formation of the CeO_2-ZrO_2-MnO_2 solid solution, the abundant active groups adsorbed on the catalyst surface, and the useful texture properties, with high dispersion of cerium, zirconium, and manganese. The mechanisms of the simultaneous oxidation of Hg^0 and NH_3-SCR of NO over $Ce_{0.47}Zr_{0.22}Mn_{0.31}O_2$ were suggested that Hg^0 oxidation and NO conversion were aided by the synergetic effect on the mobility of surface oxygen and the activation of lattice oxygen. Especially, the interaction between NH_3-SCR and Hg^0 oxidation was inferred that adsorbed Hg^0/Hg^{2+} occupied the surface active sites of the catalyst, which might abate the formation of $NH_{3(ad)}$, $-NH_{2(ad)}$, and NH_4^+ on acid sites. Ultimately, it led to the inhibition of NO conversion. Similar, the negative effect of NH_3-SCR of NO on Hg^0 oxidation was not obvious at low temperature.

References

Aghazadeha M, Maragheh MG, Ganjali MR, Norouzi P, Faridbod F (2016) Electrochemical preparation of MnO_2 nanobelts through pulse base-electrogeneration and evaluation of their electrochemical performance. Appl Surf Sci 364:141–147 Article CAS Google Scholar

Bin F, Song C, Lv G, Song J, Wu S, Li X (2014) Selective catalytic reduction of nitric oxide with ammonia over zirconium-doped copper/ZSM-5 catalysts. Appl Catal B Environ 150:532–543 Article CAS Google Scholar

Boningari T, Smirniotis PG (2016) Impact of nitrogen oxides on the environment and human health: Mn-based materials for the NOx abatement. Cur Opin Chem Eng 13:133–141 Article Google Scholar

Boningari T, Ettireddy PR, Somogyvari A, Liu Y, Vorontsov A, Mcdonald CA et al (2015) Influence of elevated surface texture hydrated titania on Ce-doped Mn/Tio_2, catalysts for the low-temperature SCR of NO_x, under oxygen-rich conditions. J Catal 325:145–155 Article CAS Google Scholar

Chi G, Shen B, Yu R, He C, Zhang X (2017) Simultaneous removal of NO and Hg^0 over Ce-Cu modified V_2O_5/TiO_2 based commercial SCR catalysts. J Hazard Mater 330:83–92 Article CAS Google Scholar

Ding S, Liu F, Shi X, Liu K, Lian Z, Xie L, He H (2015) Significant promotion effect of Mo additive on novel Ce-Zr mixed oxide catalyst for the selective catalytic reduction of NO_x with NH_3. ACS Appl Mater Interfaces 7:9497 Article CAS Google Scholar

Ettireddy PR, Ettireddy N, Mamedov S, Boolchand P, Smirniotis PG (2007) Surface characterization studies of TiO_2 supported manganese oxide catalysts for low temperature SCR of NO with NH_3. Appl Catal B Environ 76:123–134 Article CAS Google Scholar

Ettireddy PR, Ettireddy N, Boningari T, Pardemann R, Smirniotis PG (2012) Investigation of the selective catalytic reduction of nitric oxide with ammonia over Mn/TiO_2, catalysts through transient isotopic labeling and in situ, FT-IR studies. J Catal 292:53–63 Article CAS Google Scholar

Fan X, Li C, Zeng G, Zhang X, Tao S, Lu P, Tan Y, Luo D (2012) Hg^0 removal from simulated flue gas over CeO_2/HZSM-5. Energy Fuel 26:2082–2089 Article CAS Google Scholar

Fang J, Bi X, Si D, Jiang Z, Huang W (2007) Spectroscopic studies of interfacial structures of CeO_2-TiO_2 mixed oxides. Appl Surf Sci 253:8952–8961 Article CAS Google Scholar

Fang P, Cen CP, Wang XM, Tang ZJ, Tang ZX, Chen DS (2013) Simultaneous removal of SO_2, NO and Hg^0 by wet scrubbing using urea + $KMnO_4$ solution. Fuel Process Technol 106:645–653 Article CAS Google Scholar

Gao X, Jiang Y, Zhong Y, Luo Z, Cen K (2010) The activity and characterization of CeO_2-TiO_2 catalysts prepared by the sol-gel method for selective catalytic reduction of NO with NH_3. J Hazard Mater 174:734–739 Article CAS Google Scholar

He J, Reddy GK, Thiel SW, Smirniotis PG, Pinto NG (2011) Ceria-modified manganese oxide/titania materials for removal of elemental and oxidized mercury from flue gas. J Phys Chem C 115:24300–24309 Article CAS Google Scholar

He J, Reddy GK, Thiel SW, Smirniotis P, Pinto NG (2013) Simultaneous removal of elemental mercury and no from flue gas using CeO_2 modified $MnOx/TiO_2$ materials. Energy Fuel 27:4832–4839 Article CAS Google Scholar

He C, Shen B, Chen J, Cai J (2014) A novel Ce-Ta mixed oxide catalyst for the selective catalytic reduction of NO_x with NH_3. Environ Sci Technol 48:7891–7898 Article CAS Google Scholar

Lei J, Sreekanth PM, Smirniotis PG, Thiel SW, Pinto NG (2008) Manganese oxide/titania materials for removal of no, x, and elemental mercury from flue gas. Energy Fuel 22:2299–2306 Article CAS Google Scholar

Li J, Chang H, Ma L, Hao J, Yang RT (2011) Low-temperature selective catalytic reduction of NO_x, with NH_3, over metal oxide and zeolite catalysts—a review. Catal Today 175:147–156 Article CAS Google Scholar

Li H, Wu S, Li L, Wang J, Ma W, Shih K (2015) CuO-CeO_2/TiO_2 catalyst for simultaneous NO reduction and Hg0 oxidation at low temperatures. Catal Sci Technol 5:5129–5138 Article CAS Google Scholar

Lian Z, Liu F, He H (2014) Enhanced activity of Ti-modified V_2O_5/CeO_2 catalyst for the selective catalytic reduction of NO_x with NH_3. Ind Eng Chem Res 53:19506–19511 Article CAS Google Scholar

Liu C, Chen L, Chang H, Ma L, Peng Y, Arandiyan H, Li J (2013) Characterization of CeO_2-WO_3 catalysts prepared by different methods for selective catalytic reduction of NO_x with NH_3. Catal Commun 40:145–148 Article CAS Google Scholar

Liu B, Huang C, Ke Y, Wang W, Kuo H, Lin D, Lin V, Lin S (2017) Enhanced selective catalytic reduction of NO over Mn-Ce catalysts with the acetic-acid-chelated titania support at low temperature. Appl Catal A Gen 538:74–80 Article CAS Google Scholar

Ma Y, Mu B, Yuan D, Zhang H, Xu H (2017) Design of MnO_2/CeO_2-MnO_2 hierarchical binary oxides for elemental mercury removal from coal-fired flue gas. J Hazard Mater 333:186–193 Article CAS Google Scholar

Marzouk MA, ElBatal FH, Morsi RMM (2017) Optical and FTIR absorption spectra of CeO_2-doped cadmium borate glasses and effects of gamma irradiation. SILICON 9:105–110 Article CAS Google Scholar

Mullins DR, Overbury SH, Huntley DR (1998) Electron spectroscopy of single crystal and polycrystalline cerium oxide surfaces. Surf Sci 409:307–319 Article CAS Google Scholar

Ozkan US, Cai Y, Kumthekar MW (1994) Investigation of the reaction pathways in selective catalytic reduction of no with NH_3 over V_2O_5 catalysts: isotopic labeling studies using $^{18}O_2$, $^{15}NH_3$, ^{15}NO, and $^{15}N^{18}O_1$. J Catal 149:375 Article CAS Google Scholar

Padmanathan N, Selladurai S (2014) Electrochemical capacitance of porous NiO-CeO_2 binary oxide synthesized via sol–gel technique for supercapacitor. Ionics 20:409–420 Article CAS Google Scholar

Pappas DK, Boningari T, Boolchand P, Smirniotis PG (2016) Novel manganese oxide confined interweaved titania nanotubes for the low-temperature selective catalytic reduction (SCR) of NO_X, by NH_3. J Catal 334:1–13 Article CAS Google Scholar

Peng Y, Qu R, Zhang X, Li J (2013) The relationship between structure and activity of MoO_3-CeO_2 catalysts for NO removal: influences of acidity and reducibility. Chem Commun 49:6215–6217 Article CAS Google Scholar

Picasso G, Gutierrez M, Pina MP, Herguido J (2007) Preparation and characterization of Ce-Zr and Ce-Mn based oxides for *n*-hexane combustion: application to catalytic membrane reactors. Chem Eng J 126:119–130 Article CAS Google Scholar

Qu R, Gao X, Cen K, Li J (2013a) Relationship between structure and performance of a novel cerium-niobium binary oxide catalyst for selective catalytic reduction of NO with NH3. Appl Catal B Environ 142–143:290–297 Article CAS Google Scholar

Qu R, Gao X, Li KJ (2013b) Relationship between structure and performance of a novel cerium-niobium binary oxide catalyst for selective catalytic reduction of NO with NH_3. Appl Catal B Environ 142–143:290–297 Article CAS Google Scholar

Reddy BM, Khan A, Lakshmanan P, Aouine M, Loridant S, Volta JC (2005) Structural characterization of nanosized CeO_2-SiO_2, CeO_2-TiO_2, and CeO_2-ZrO_2 catalysts by XRD, Raman, and HREM techniques. J Phys Chem B 109:3355–3363 Article CAS Google Scholar

Reddy GK, He J, Thiel SW, Pinto NG, Smirniotis PG (2015) Sulfur-tolerant Mn-Ce-Ti sorbents for elemental mercury removal from flue gas: mechanistic investigation by XPS. J Phys Chem C 119:8634–8644 Article CAS Google Scholar

Rivas B, López-Fonseca R, González-Velasco JR, Gutiérrez-Ortiz JI (2008) Adsorption and oxidation of trichloroethylene on Ce/Zr mixed oxides: in situ FTIR and flow studies. Catal Commun 9:2018–2021 Article CAS Google Scholar

Santos MLD, Lima RC, Riccardi CS, Tranquilin RL, Bueno PR, Varela JA, Longo E (2008) Preparation and characterization of ceria nanospheres by microwave-hydrothermal method. Mater Lett 62:4509–4511 Article CAS Google Scholar

Schmitt J, Flemming HC (1998) FTIR-spectroscopy in microbial and material analysis. Int Biodeterior Biodegrad 41:1–11 Article CAS Google Scholar

Sjostrom S, Durham M, Bustard CJ, Martin C (2010) Activated carbon injection for mercury control: overview. Fuel 89:1320–1322 Article CAS Google Scholar

Smirniotis PG, Peña DA, Uphade BS (2001) Low-temperature selective catalytic reduction (SCR) of NO with NH(3) by using Mn, Cr, and Cu oxides supported on hombikat Tio(2). Angew Chem Int Ed Engl 40:2479–2482 Article CAS Google Scholar

Song Z, Ning P, Zhang Q, Li H, Zhang J, Wang Y, Liu X, Huang Z (2016) Activity and hydrothermal stability of CeO_2-ZrO_2-WO_3 for the selective catalytic reduction of NO_x with NH_3. J Environ Sci 42:168–177 Article Google Scholar

Tompsett DA, Parker S,C, Islam MS (2014) Surface properties of α-MnO_2: relevance to catalytic and supercapacitor behavior. J Mater Chem A 2: 15509–15518.

Wang Y, Shen B, He C, Yue S, Wang F (2015) Simultaneous removal of NO and Hg^0 from flue gas over Mn–Ce/Ti-PILCs. Environ Sci Technol 49:9355–9363 Article CAS Google Scholar

Wang S, Guo R, Pan W, Chen Q, Sun P, Li M, Liu S (2017) The deactivation of Ce/TiO_2 catalyst for NH3-SCR reaction by alkali metals: TPD and DRIFT studies. Catal Commun 89:143–147 Article CAS Google Scholar

Watanabe S, Ma X, Song C (2009) Characterization of structural and surface properties of nanocrystalline TiO_2-CeO_2 mixed oxides by XRD, XPS, TPR, and TPD. J Phys Chem C 113:14249–14257 Article CAS Google Scholar

Wen X, Li C, Fan X, Gao H, Zhang W, Chen L, Zeng G, Zhao Y (2011) Experimental study of gaseous elemental mercury removal with CeO_2/γ-Al_2O_3. Energy Fuel 25:2939–2944 Article CAS Google Scholar

Xie J, Qu Z, Yan N, Yang S, Chen W, Hu L, Huang W, Liu P (2013) Novel regenerable sorbent based on Zr–Mn binary metal oxides for flue gas mercury retention and recovery. J Hazard Mater 261:206–213 Article CAS Google Scholar

Xu H, Qu Z, Zhao S, Mei J, Quan F, Yan N (2015) Different crystal-forms of one-dimensional MnO_2 nanomaterials for the catalytic oxidation and adsorption of elemental mercury. J Hazard Mater 299:86–93 Article CAS Google Scholar

Yang S, Zhu W, Jiang Z, Chen Z, Wang J (2006) The surface properties and the activities in catalytic wet air oxidation over CeO_2-TiO_2 catalysts. Appl Surf Sci 252:8499–8505 Article CAS Google Scholar

Yang S, Wang C, Li J, Yan N, Ma L, Chang H (2011) Low temperature selective catalytic reduction of NO with NH_3 over Mn-Fe spinel: performance, mechanism and kinetic study. Appl Catal B Environ 110:71–80 Article CAS Google Scholar

Yang J, Zhao Y, Chang L, Zhang J, Zheng C (2015) Mercury adsorption and oxidation over cobalt oxide loaded magnetospheres catalyst from fly ash in oxyfuel combustion flue gas. Environ Sci Technol 49:8210–8218 Article CAS Google Scholar

Younes MK, Ghorbel A, Rives A, Hubaut R (2003) Comparative study of the acidity of sulphated zirconia supported on alumina prepared by sol-gel and impregnation methods. J Sol-Gel Sci Technol 26:677–680 Article CAS Google Scholar

Yuan Y, Zhang JY, Li HL, Li Y, Zhao YC, Zheng CG (2012) Simultaneous removal of SO_2, NO and mercury using TiO_2-aluminum silicate fiber by photocatalysis. Chem Eng J 192:21–28 Article CAS Google Scholar

Zhang Q, Pan W, Guo R (2013) The research of SCR catalyst for elemental mercury conversion in coal-fired flue gas. Adv Mater Res 864–867:1470–1473 Article CAS Google Scholar

Zhang L, Li L, Cao Y, Yao X, Ge C, Gao F, Deng Y, Tang C, Dong L (2015a) Getting insight into the influence of SO_2 on TiO_2/CeO_2 for the selective catalytic reduction of NO by NH_3. Appl Catal B Environ 165:589–598 Article CAS Google Scholar

Zhang T, Qu R, Su W, Li J (2015b) A novel Ce-Ta mixed oxide catalyst for the selective catalytic reduction of NO_x with NH_3. Appl Catal B Environ 176–177:338–346 Article CAS Google Scholar

Zhang X, Li C, Zhao L, Zhang J, Zeng G, Xie Y, Yu M (2015c) Simultaneous removal of elemental mercury and NO from flue gas byV_2O_5-CeO_2/TiO_2 catalysts. Appl Surf Sci 347:392–400 Article CAS Google Scholar

Zhang J, Li C, Zhao L, Wang T, Li S, Zeng G (2017a) A sol-gel Ti-Al-Ce-nanoparticle catalyst for simultaneous removal of NO and Hg^0 from simulated flue gas. Chem Eng J 313:1535–1547 Article CAS Google Scholar

Zhang X, Cui Y, Wang J, Tan B, Li C, Zhang H, He G (2017b) Simultaneous removal of Hg^0 and NO from flue gas by $Co_{0.3}$-$Ce_{0.35}$-$Zr_{0.35}O_2$ impregnated with MnO_x. Chem Eng J 326:1210–1222 Article CAS Google Scholar

Zhao Y, Hao R, Qi M (2015) Integrative process of peroxidation and absorption for simultaneous removal of SO_2, NO and Hg^0. Chem Eng J 269:159–167 Article CAS Google Scholar

Zhao L, Li C, Li S, Wang Y, Zhang J, Wang T, Zeng G (2016a) Simultaneous removal of elemental mercury and NO in simulated flue gas over V_2O_5/ZrO_2-CeO_2catalyst. Appl Catal B Environ 198:420–430 Article CAS Google Scholar

Zhao Y, Hao R, Yuan B, Jiang J (2016b) Simultaneous removal of SO_2, NO and Hg^0 through an integrative process utilizing a cost-effective complex oxidant. J Hazard Mater 301:74–83 Article CAS Google Scholar

Zheng L, Liu G, Chou C (2007) The distribution, occurrence and environmental effect of mercury in Chinese coals. Sci Total Environ 384:374–383 Article CAS Google Scholar

Zhu H, Qin Z, Shan W, Shen W, Wang J (2004) Pd/CeO_2-TiO_2 catalyst for CO oxidation at low temperature: a TPR study with H_2 and CO as reducing agents. J Catal 225:267–277 Article CAS Google Scholar